Journal of Glaciology



Article

Cite this article: Schroeder DM, May DF and Pranis O (2026) Waveform choice in ice-penetrating radar. *Journal of Glaciology* **72**, e88, 1–11. https://doi.org/10.1017/jog.2026.10210

Received: 26 March 2026 UTC
Revised: 6 August 2026 UTC
Accepted: 11 August 2026 UTC

Keywords:
glaciological instruments and methods; ground-penetrating radar; radio-echo sounding

Corresponding author: Dustin M. Schroeder; Email: dustin.m.schroeder@stanford.edu

© The Author(s), 2026. Published by Cambridge University Press on behalf of International Glaciological Society. This is an Open Access article, distributed under the terms of the Creative Commons Attribution licence (http://creativecommons.org/licenses/by/4.0), which permits unrestricted re-use, distribution and reproduction, provided the original article is properly cited.

Waveform choice in ice-penetrating radar

Dustin M. Schroeder[1,2], Daniel F. May[1] and Oliver Pranis[2]

[1]Department of Geophysics, Stanford University, Stanford, CA, USA and [2]Department of Electrical Engineering, Stanford University, Stanford, CA, USA

Abstract

There is a growing collection of ice-penetrating radar systems being used in a variety of glaciological settings to collect a body of data that is expanding in its scale, diversity and information richness. While there are nuanced differences among particular instruments, there are four main classes of radar systems used to observe the subsurface of ice sheets and glaciers: monotone pulse airborne sounders, chirped airborne sounders, ground-traversed impulsive systems and stationary continuous-wave systems. While these classes are often treated as fundamentally different instruments with distinct communities and literature, we seek to reframe them as choices on a continuum of potential waveforms. In particular, we focus on the tradeoff between achieving large coherent processing gains and mitigating interference from the matched-filter response of strong echoes at shorter delays as the key limiting factors for subsurface target detection. We also discuss the glaciological settings in which different waveform choices perform best, as well as potential avenues this raises for new instrument and experiment designs.

Introduction

Ice-penetrating radar systems are one of the primary geophysical instruments in field-based studies of glaciers and ice sheets (Schroeder and others, 2020). Beyond their widespread and growing use, these instruments are the subject of study and innovation in and of themselves and have increased in variety and capability in recent years (Allen, 2008; Dall, 2010; Paden and others, 2010; Brennan and others, 2014; Arnold and others, 2020; Mingo and others, 2020; Scanlan and others, 2020; Peters and others, 2021; Teisberg and others, 2024). For the purposes of this paper, we group the most common types of ice-penetrating radars used across glaciology into four categories:

- **Monotone Pulse Radar Sounders** like the incoherent system operated during the original SPRI-NSF-TUD surveys in the 1960s and 70s, but largely unused since then (Bailey and others, 1964; Christensen and others, 1970).
- **Chirped Radar Sounders** like HiCARS, MCoRDS, PASIN and similar modern airborne systems (Peters and others, 2007; Rodriguez-Morales and others, 2013; Arenas-Pingarrón and others, 2023).
- **Impulsive Ice-Penetrating Radars** which are or are similar to commercial Ground Penetrating Radars (GPRs) (Arcone and others, 2004; Björnsson and Pálsson, 2020; Mingo and others, 2020).
- **Continuous Wave Radars** typically operated in stationary in situ deployments like the ApRES system (Brennan and others, 2014; Nicholls and others, 2015; Bienert and others, 2020).

Although there are instruments and communities of practice that have evolved around each of these categories, we seek to show that these systems can be viewed on a continuum in terms of their waveforms and how the properties of particular glaciological targets and acquisition platforms can both explain and inform the choices that have and can be made in terms of their selection, configuration or design.

Waveform description

In this paper, we describe transmitted radar waveforms in terms of parameter choices modifying a single generic Linearly Frequency Modulated (LFM) or 'chirped' waveform. Figure 1a shows an LFM waveform with amplitude A and pulse length L that is windowed by function $w(t)$.

https://doi.org/10.1017/jog.2026.10210 Published online by Cambridge University Press

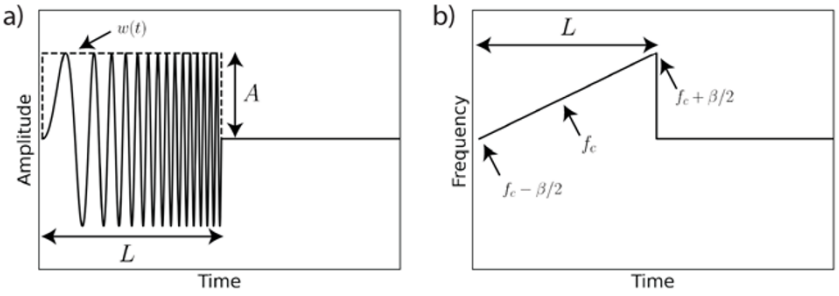


Figure 1. A generic LFM waveform $s(t)$ with length L, amplitude A, center frequency f_c, bandwidth β and windowed by function $w(t)$.

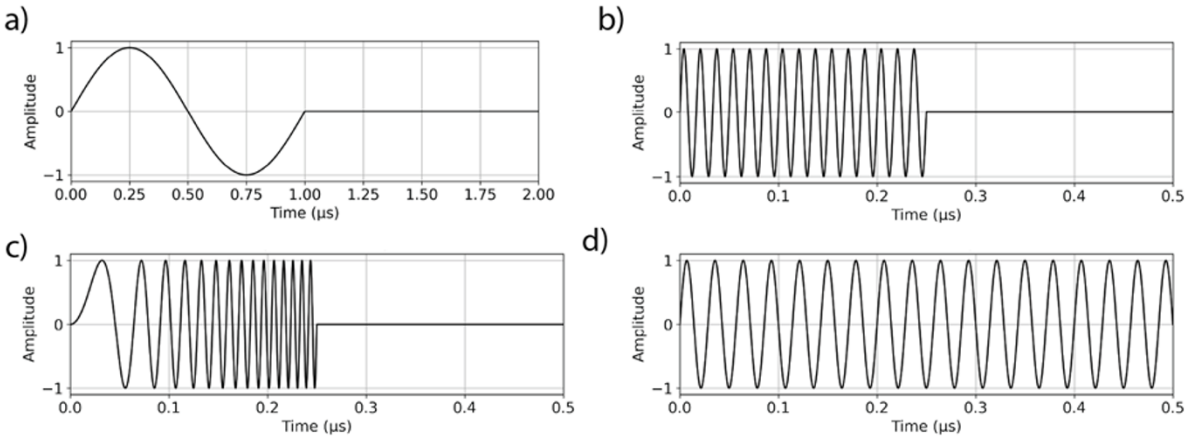


Figure 2. By selecting β, f_c and L appropriately, we can approximate waveforms like (a) an impulse-like radar, (b) a monotone pulse-like radar, (c) an LFM chirp-like radar and (d) a CW-like radar.

Figure 1b shows its corresponding sweep of frequency across a bandwidth of β with a center frequency of f_c. The amplitude of this waveform $s(t)$ is given by

$$s(t) = w(t) \exp\left\{j\left(2\pi f_c t - \pi k L t + \pi k t^2\right)\right\}. \quad (1)$$

where $k = \beta/L$ is the chirp rate and $w(t)$ is a Kaiser window described by

$$w(t) = \frac{I_0\left(\pi\alpha\sqrt{1-(\frac{2t}{L}-1)^2}\right)}{I_0(\pi\alpha)}, \quad (2)$$

where α is the Kaiser window shape parameter and $I_0(\cdot)$ is a zeroth-order modified Bessel Function of the first kind.

Figure 2 shows how impulsive, monotone, chirped and continuous wave signals can all be approximated by the generic LFM waveform shown in Fig. 1 through the choice of different parameter values. For example, Fig. 2a shows that a short value of L relative to $1/f_c$ can result in impulsive or bicyclic GPR-like waveforms. Similarly, Fig. 2b shows that a monotone pulse waveform can be produced by setting β to zero.[1] Figure 2c shows a canonical chirp of the kind used in most modern airborne and space-borne radar sounders. Finally, Fig. 2d shows that waveforms with large values of L can behave like Continuous Wave (CW) radar in that the signal from the surface is still being received at the same delay as echoes from the bed (Brennan and others, 2014).

Figure 3 is a conceptual plot that illustrates the regimes for which the chirp in Fig. 1 will behave more like each of the four classes of penetrating radar waveforms. This depends on the choice of β and L relative to the center frequency f_c and delay between the surface and bed τ_b.[2] For example, waveforms with values of L near or below the carrier period $1/f_c$ will result in impulse-like waveforms and those with values of L longer than the bed echo delay τ_b produce CW-like waveforms. For intermediate length pulses, chirp-like waveforms will be produced when $\beta > 1/L$ and monotone-like pulses will be produced when $\beta < 1/L$.

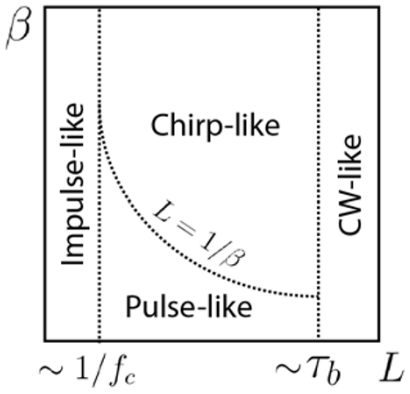


Figure 3. Using the generic LFM pulsed waveform illustrated in Fig. 1, the choices of β, L and f_c can approximate the behavior of bicyclic impulse GPR-like, chirp-like, monotone pulse-like and CW-like waveforms.

[1]Note that this is the parameter β in the LFM sweep and that the effective bandwidth β_{eff} of the monotone pulse is instead determined by the pulse length and equal to $1/L$.

[2]Again, we note that β on the y-axis of Fig. 3 is the range of frequency in the FMCW waveform Equation 1 and not the net effective bandwidth of the waveform β_{eff} which is determined by a combination of β, L and $w(t)$.

https://doi.org/10.1017/jog.2026.10210 Published online by Cambridge University Press

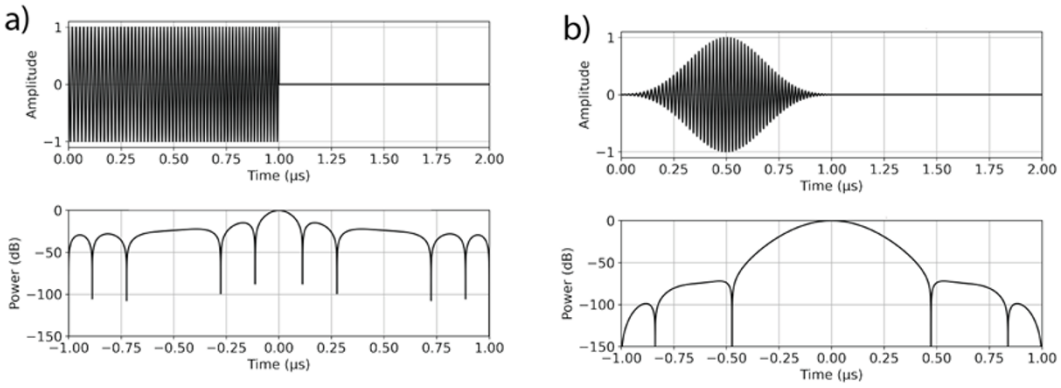


Figure 4. The Kaiser Window can approximate (a) a rectangular window ($\alpha \approx 0$), (b) a Blackman-Harris window ($\alpha \approx 7$) or other commonly used window functions based on the choice of α. The upper row shows the windowed waveform and the lower row shows the windowed waveform after pulse compression via matched filtering.

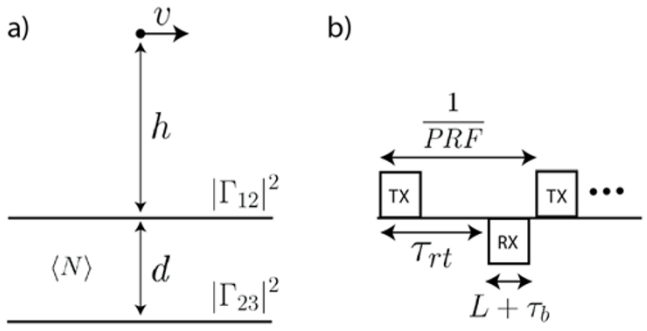


Figure 5. (a) A representative acquisition geometry in terms of the platform speed v, survey height h, the depth of the subsurface target d, the one-way depth-averaged attenuation rate $\langle N \rangle$ in dB/km and the Fresnel reflection coefficients of the surface $|\Gamma_{12}|^2$ and of the bed $|\Gamma_{23}|^2$ and (b) timing diagram with transmit (TX) and receive (RX) windows for ice-penetrating radar observations in terms of the round-trip time between the platform and the surface τ_{rt}, the round-trip delay between the surface and the bed τ_b, the pulse length L and the PRF.

In addition to the choice between bandwidth and pulse-length illustrated in Fig. 3, some of the waveforms used in glaciology also use non-rectangular window functions $w(t)$ which can have a significant effect on waveform performance. Figure 4 shows the Kaiser window described by Equation 2, for which a single parameter α can approximate a range of window functions spanning from a rectangular window (for $\alpha \approx 0$), to a Hamming window ($\alpha \approx 2.5$) or to a Blackman-Harris window ($\alpha \approx 7$). Taken together, the choices of α, β, L and f_c are sufficient for our description and exploration of waveform choice.

Target and platform description

Just as the previous section described typical radar systems in terms of four waveform parameters, this section seeks to describe the range of acquisition geometries, platforms and targets in a similarly economical set. Figure 5a illustrates the acquisition geometry for generic ice-penetrating radar observations, which can be described by the platform height above the ice surface h, the speed of the platform v, the depth to a subsurface target d, the one-way depth-averaged attenuation rate $\langle N \rangle$ in dB/km and the Fresnel reflection coefficients of the surface $|\Gamma_{12}|^2$ and of the bed $|\Gamma_{23}|^2$.

For our purposes, we are only concerned with the two primary ways in which waveform choice affects the detectability of a subsurface interface:

- Overlap of the matched-filter response of the ice surface with the return from the bed.
- Noise floor power that exceeds the power of the bed echo.

As a result, we can further reduce the parameters in Fig. 5a to those shown in Fig. 6, specifically the delay between surface and bed echoes τ_b, the difference in returned power between the surface and the bed $[\Delta P_r]$ and the Signal-to-Noise Ratio of a single unprocessed bed echo relative to an additive Gaussian white (AGW) noise floor $[\text{SNR}_0]$, which are given

$$\tau_b = \frac{2d\sqrt{\epsilon_i}}{c}, \tag{3}$$

and

$$[\Delta P_r] = [|\Gamma_{12}|^2] - [|\Gamma_{23}|^2] + 2d\,\langle N \rangle\,, \tag{4}$$

where $[\cdot]$ indicates power units in dB so that $[x] = 10\log_{10}(x)$.

For this target description, the returned signal $r(t)$ will be

$$r(t) = s(t) + \frac{1}{\sqrt{\Delta P_r}} s(t - \tau_b) + n(t) \tag{5}$$

where ϵ_i is the real permittivity of ice, d is the depth of ice, c is the speed of light, ΔP_r (in linear units) is the ratio between the surface echo power P_{surf} and bed echo power P_{bed} and $n(t)$ is a single realization of band-limited white noise with an rms amplitude σ_n of

$$\sigma_n = \sqrt{\frac{\beta/\beta_0}{\text{SNR}_0 \Delta P_r}} \tag{6}$$

where β_0 is the arbitrary reference bandwidth (we use $\beta_0 = 1$ MHz) at which SNR_0 is defined. We note that Equation 5 is referenced to the surface echo in both delay and amplitude so that the surface echo $s(t)$ has unit amplitude and occurs at time $t = 0$. As a result, the single-pulse SNR of the bed echo before matched filtering, SNR_0 (in linear units), is

$$\text{SNR}_0 = \frac{P_{\text{bed}}}{P_{\text{noise}}}, \tag{7}$$

where P_{noise} is the power of band-limited Gaussian white noise $n(t)$

$$P_{\text{noise}} = \sigma_n^2. \tag{8}$$

The acquisition platform is entirely described by v and h.

https://doi.org/10.1017/jog.2026.10210 Published online by Cambridge University Press

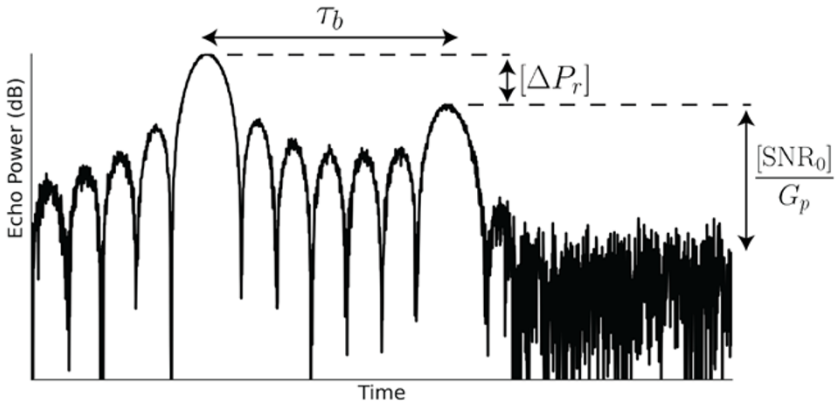


Figure 6. The key parameters that define the target in terms of the way it governs the relative limitations on bed echo detection from surface side lobes and the additive noise floor are d, ΔP_r and SNR_0. G_c is the pulse compression gain and is a direct result of the matched filtering of the waveform.

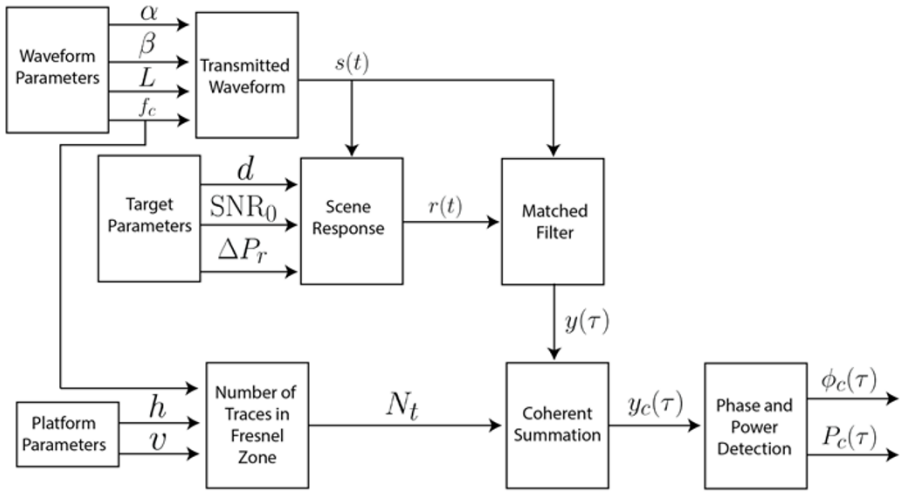


Figure 7. Flowchart illustrating the processing pipeline by which the selection of waveform parameters (α,β,L,f_c), target parameters (d, SNR_0, ΔP_r) and platform parameters (h,v) determine the processed power $P_c(\tau)$ and phase $\phi(\tau)$ performance in ice-penetrating radar systems.

Processing description

In order to investigate the effect of waveform choice on subsurface echo detection, we consider a single uniform processing pipeline in which the choice of waveform parameters entirely determines the performance of that waveform. Figure 7 illustrates that processing pipeline for waveform parameters (α,β,L,f_c), target parameters (d, SNR_0, ΔP_r) and platform parameters (h,v).

In this pipeline, the transmitted waveform $s(t)$ described in Equation 1 is matched filtered with the returned signal from the scene response $r(t)$ described in Equation 5 to produce a single-pulse fast-time trace $y(\tau)$ given by

$$y(\tau) = \int r(t)s^*(t-\tau)dt, \tag{9}$$

where $s(t)^*$ is the complex conjugate of $s(t)$. For the target scene parameters in Fig. 6, the single-pulse trace is

$$y(\tau) = R_s(\tau) + \frac{1}{\sqrt{\Delta P_r}} R_s(\tau - \tau_b) + n_m(\tau), \tag{10}$$

where $R_s(\tau)$ is the matched-filter response of the transmitted waveform,

$$R_s(\tau) = \int s(t)s^*(t-\tau)dt, \tag{11}$$

and $n_m(\tau)$ is the matched-filter noise and given by

$$n_m(\tau) = \int n(t)s^*(t-\tau)dt. \tag{12}$$

These traces are then coherently summed across a Fresnel zone diameter D_f to increase bed echo power relative to the noise floor so that the number of traces available for coherent summation N_t is

$$N_t = \lfloor \frac{D_f \mathrm{PRF}}{v} \rfloor, \tag{13}$$

where $\lfloor \cdot \rfloor$ notates the floor and PRF is the pulse repetition frequency which is limited by

$$\mathrm{PRF} \leq \frac{1}{L + \tau_b + \tau_{rt}}, \tag{14}$$

where τ_{rt} is the round-trip time between the platform and ice surface, given by

$$\tau_{rt} = \frac{2h}{c}. \tag{15}$$

After coherent summation, the surface-echo-normalized power profile $[P_c(\tau)]$ (in dB) becomes

$$[P_c(\tau)] = 10\log_{10}(|y_c(\tau)|^2), \tag{16}$$

where

$$y_c(\tau) = \frac{R_s(\tau)}{R_s(0)} + \frac{1}{\sqrt{\Delta P_r}} \frac{R_s(\tau - \tau_b)}{R_s(0)} + n_{m,c}(\tau), \tag{17}$$

and

$$n_{m,c}(\tau) = \frac{1}{R_s(0)} \int n_c(t)s^*(t-\tau)dt. \tag{18}$$

https://doi.org/10.1017/jog.2026.10210 Published online by Cambridge University Press

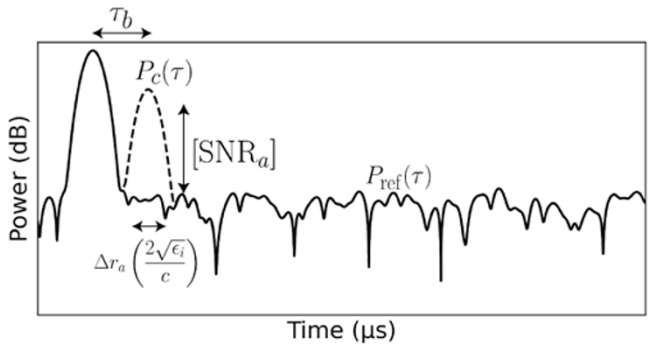


Figure 8. Illustration of the performance metrics of 'apparent' Signal-to-Noise Ratio [SNR$_a$] and 'apparent' range resolution Δr_a. Both lines include the contribution of the surface matched-filter response and an additive noise floor. Only the dashed line also includes the echo from the subsurface target.

After coherent summation, $n_c(t)$ has an RMS amplitude $\sigma_{n,c}$ given by

$$\sigma_{n,c} = \sqrt{\frac{\beta/\beta_0}{\text{SNR}_0 N_t \Delta P_r}}. \tag{19}$$

The normalized matched-filter noise after coherent summation $n_{m,c}(\tau)$ has an RMS amplitude $\sigma_{m,c}$ given by

$$\sigma_{m,c} = \sqrt{\frac{\beta/\beta_0}{\text{SNR}_0 N_t G_c \Delta P_r}}, \tag{20}$$

where G_c is the matched-filter SNR gain experienced by our unit-peak-amplitude signal $s(t)$ during matched filtering and given by

$$G_c = \beta R_s(0) = \beta \int |s(t)|^2 \, dt \tag{21}$$

Because both the pre-matched-filter noise power and G_c scale linearly with β, the bandwidth terms cancel and, assuming additive white noise, the post-matched-filter SNR does not improve by increasing β alone.

In addition to producing the power trace $P_c(\tau)$, this pipeline also produces the phase trace $\phi(\tau)$, given by

$$\phi(\tau) = \angle y_c(\tau). \tag{22}$$

Performance description

The previous sections made the case that both radar waveforms and glaciological acquisition scenarios can be described by a small number of parameters. In order to assess the bed detection performance of waveforms across scenarios, we describe that performance in terms of two metrics: the 'apparent' Signal-to-Noise Ratio [SNR$_a$] and the 'apparent' range resolution Δr_a. As shown in Fig. 8, these describe the 'height' and 'width' of a subsurface target echo 'above' the combined background of the surface matched-filter response and the additive noise floor.

We can directly estimate these values by first simulating the power for the surface echo, bed echo and noise floor $[P_c(\tau)]$ and then subtracting a reference power trace for the surface and noise floor alone $[P_{\text{ref}}(\tau)]$ given by

$$[P_{\text{ref}}(\tau)] = 10\log_{10}(|y_{\text{ref}}(\tau)|^2) \tag{23}$$

where

$$y_{\text{ref}}(\tau) = \frac{R_s(\tau)}{R_s(0)} + n_{m,c}(\tau). \tag{24}$$

The resulting performance values [SNR$_a$] and Δr_a are the peak and full-width half-max of

$$[P_c(\tau)] - [P_{\text{ref}}(\tau)]. \tag{25}$$

Because we are interested in general waveform performance rather than simulating any single measurement realization, our analysis can and should focus on average noise power $\langle P_{\text{noise}} \rangle$ across many realizations. In particular, we are interested when bed detection transitions from noise-limited

$$\left|\frac{R_s(\tau_b)}{R_s(0)}\right|^2 < \langle P_{\text{noise}} \rangle \tag{26}$$

to matched-filter response limited

$$\left|\frac{R_s(\tau_b)}{R_s(0)}\right|^2 > \langle P_{\text{noise}} \rangle \,. \tag{27}$$

As a result, [SNR$_a$] can be estimated even more simply by considering the limit introduced by the maximum $|R_s(\tau)|$ and $\langle P_{\text{noise}} \rangle$ at τ_b or

$$10\log_{10}\left(\max\left[\left|\frac{R_s(\tau_b)}{R_s(0)}\right|^2, \langle P_{\text{noise}} \rangle\right]\right) \tag{28}$$

where

$$\langle P_{\text{noise}} \rangle = \frac{\beta/\beta_0}{\text{SNR}_0 N_t G_c \Delta P_r} \tag{29}$$

so that

$$[\text{SNR}_a] = -[\Delta P_r] - 10\log_{10}\left(\max\left[\left|\frac{R_s(\tau_b)}{R_s(0)}\right|^2, \langle P_{\text{noise}} \rangle\right]\right). \tag{30}$$

as shown in Figure 9a. Similarly, Δr_a can be estimated as the 3 dB width of $|R_s(\tau)|^2$ as shown in Figure 9b.

Results

Airborne ice-sheet sounding

Airborne sounding of ice sheets is one of the most widespread observational scenarios in radioglaciology. It was one of the first platforms and targets for ice-penetrating radar and continues to be a major focus of data acquisition (Robin and others, 1977; Pritchard and others, 2025). For this scenario, we use an aircraft speed v of 90 m/s, a survey clearance h of 500 m, a target ice depth d of 500 m, a center frequency f_c of 60 MHz, a SNR$_0$ of -50 dB, an α of 0 and a ΔP_r of 50 dB, which are within the range of typical values for an airborne platform surveying interior ice (Schroeder and others, 2021). We then evaluate the performance of different waveforms in this scenario by exploring a range of β and L values. Figure 10 shows the results for [SNR$_a$] and Δr_a. In this scenario, the apparent SNR of the bed is maximized by increasing L up to the point where it reaches τ_b. Beyond that length, the stronger surface matched-filter response overlaps the bed echo. We also see that apparent range resolution is improved by maximizing β. This corresponds well with the chirped waveforms used in most modern airborne and satellite ice-penetrating radars.

While many radar sounders transmit waveforms with rectangular windows either to maximize the transmitted energy or as a result of power amplifiers that operate in saturation, most apply window functions during pulse-compression to mitigate matched-filter response levels (Blankenship and others, 2024). Additionally, some ice-penetrating radar systems have power amplifiers that

https://doi.org/10.1017/jog.2026.10210 Published online by Cambridge University Press

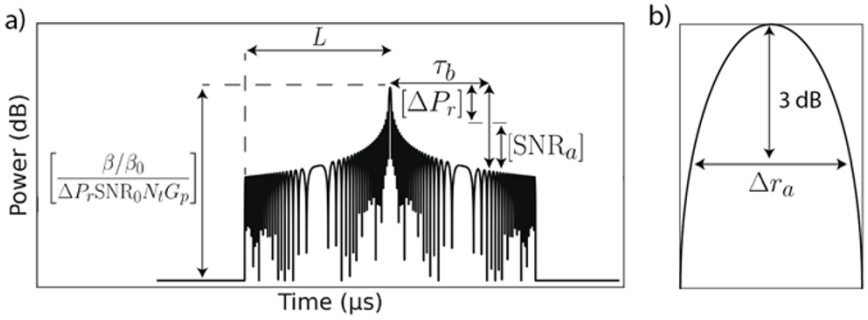


Figure 9. (a) Illustration of how the matched-filter response of the waveform $R_s(\tau)$ and the noise floor average power P_{noise} determine the apparent Signal-to-Noise Ratio $[\mathrm{SNR}_a]$ with (b) a zoomed-in illustration of the peak showing how it determines the apparent range resolution Δr_a.

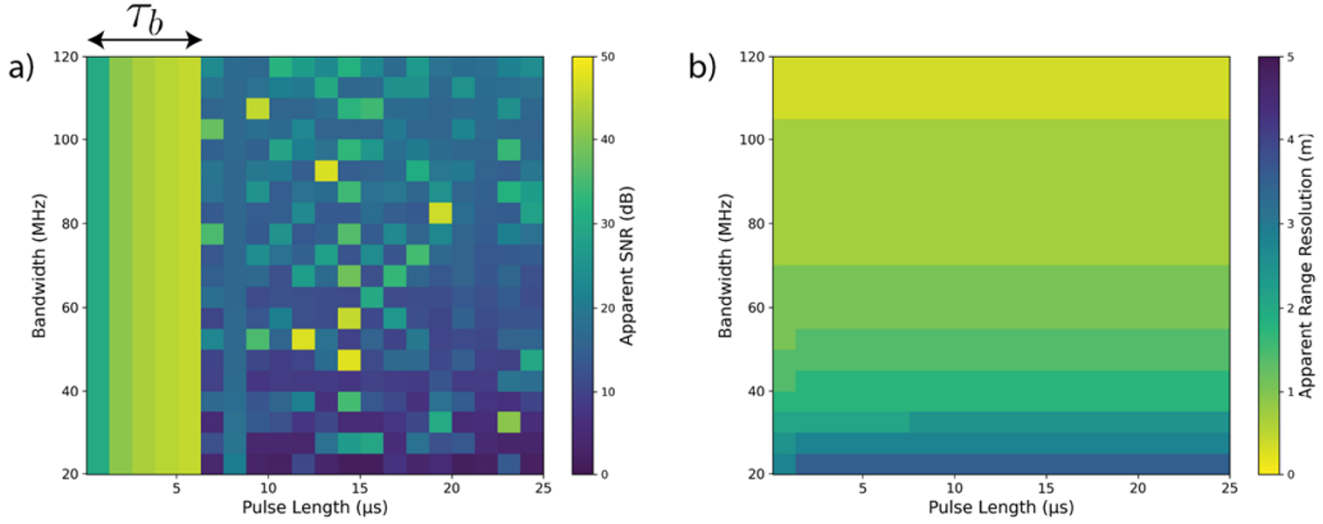


Figure 10. The performance of an airborne sounder with a rectangular window ($\alpha = 0$) in terms of (a) the apparent Signal-to-Noise Ratio $[\mathrm{SNR}_a]$ and (b) apparent range resolution Δr_a as a function of bandwidth β and pulse length L. The target/platform parameters used in this scenario were $v = 90$ m/s, $h = 500$ m, $d = 500$ m, SNR_0 = -10 dB, $\Delta P_r = 50$ dB , $f_c = 60$ MHz.

operate linearly rather than in saturation and can window waveforms both on transmit and during pulse compression, doubling the potential to shape the matched-filter response (Teisberg and others, 2024). We explore the impact of windowed waveforms in this second case by considering waveforms with $\alpha \neq 0$ in our processing pipeline. Figure 11 expands the scenario considered in Fig. 10 by varying α values. It shows that more aggressive windowing can allow longer pulses to be used, but that the improvement is stronger at certain depths and comes at the price of some energy loss and reduced range resolution.

Ground-traversed observations of temperate glaciers

Impulsive GPR-like systems are another mainstay of geophysical glaciology (Arcone and others, 2004). For this scenario, we consider a ground-traversed v of 10 m/s, an α of 0, a survey clearance h of 0 m for a system on the ice surface, a target ice depth d of 100 m, a center frequency f_c of 1 MHz, an SNR_0 of 1 dB and a ΔP_r of 20 dB, all of which fall within the range of plausible values for a temperate glacier survey. Figure 12 shows that for this scenario, the optimal pulse length is dramatically shorter than in the chirped scenario since the thinner depth makes it easy for the surface matched-filter response to overlap the bed echo. We note that for ground-traversed observing scenarios, the direct-path signal (air wave) rather than the surface reflection may be the source of the obscuring matched-filter response, but the effect and conclusions are the same. Figure 12b also shows that the apparent range resolution is determined by pulse length. This is consistent with impulsive waveforms used in ground-traversed GPRs that are commonly used to image beneath thinner ice masses like temperate glaciers.

Stationary ground-based observations

In addition to the long-established chirped and impulsive systems, a growing number of ice-penetrating radar observations are being collected using stationary systems which are deployed for long periods of time on the surface of ice sheets (Nicholls and others, 2015). For this scenario, we use a survey clearance h of 0 m, a target ice depth d of 1.2 km, a center frequency f_c of 300 MHz, an α value of 0, a SNR_0 of -30 dB and a ΔP_r of 40 dB, all within the range of typical values for interior ice (Schroeder and others, 2021). Additionally, for this type of observation, we consider two cases: a comparatively low SNR case and a comparatively high SNR case.

Low SNR case

For the case of an observation with a low post-processing SNR, we consider a v of 0.1 m/s, which would correspond to summing pulses over a few minutes to keep the noise floor the primary obstacle for bed echo detection. Figure 13 shows that the SNR-maximizing choice for this scenario is to have a waveform 'as long as possible'. Similarly, the resolution-maximizing choice is to have a waveform with as wide a bandwidth as possible. This is entirely

https://doi.org/10.1017/jog.2026.10210 Published online by Cambridge University Press

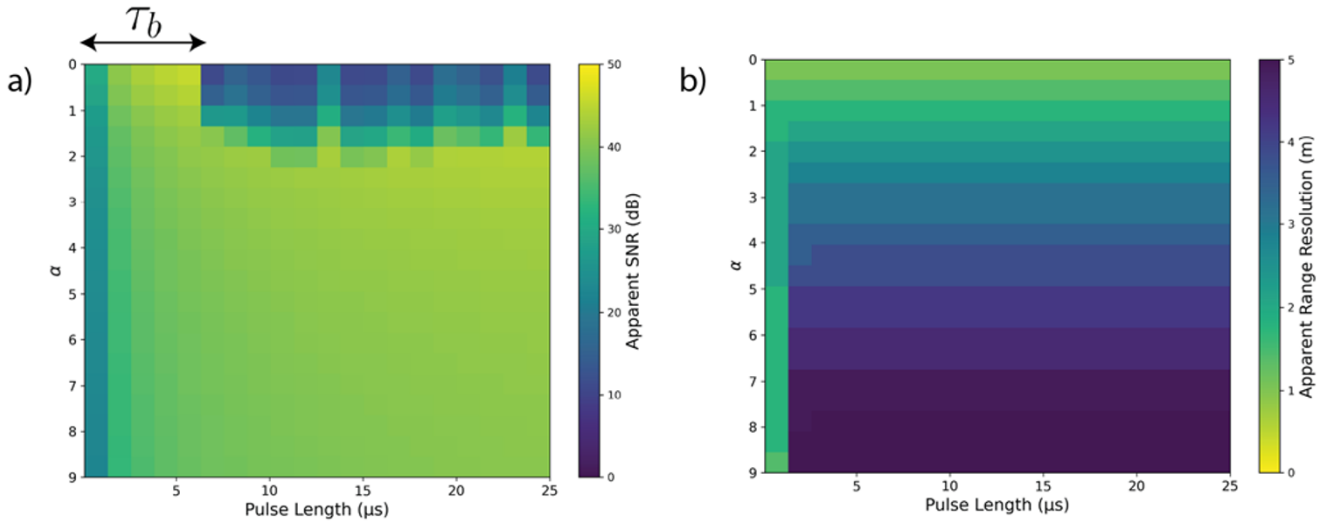


Figure 11. The performance of an airborne sounding with Kaiser window applied on transmit and during pulse compression. (a) The apparent $[\mathrm{SNR}_a]$ and (b) apparent range resolution Δr_a as a function of Kaiser window parameter α and pulse length L. The target/platform parameters match those used in Figure 10.

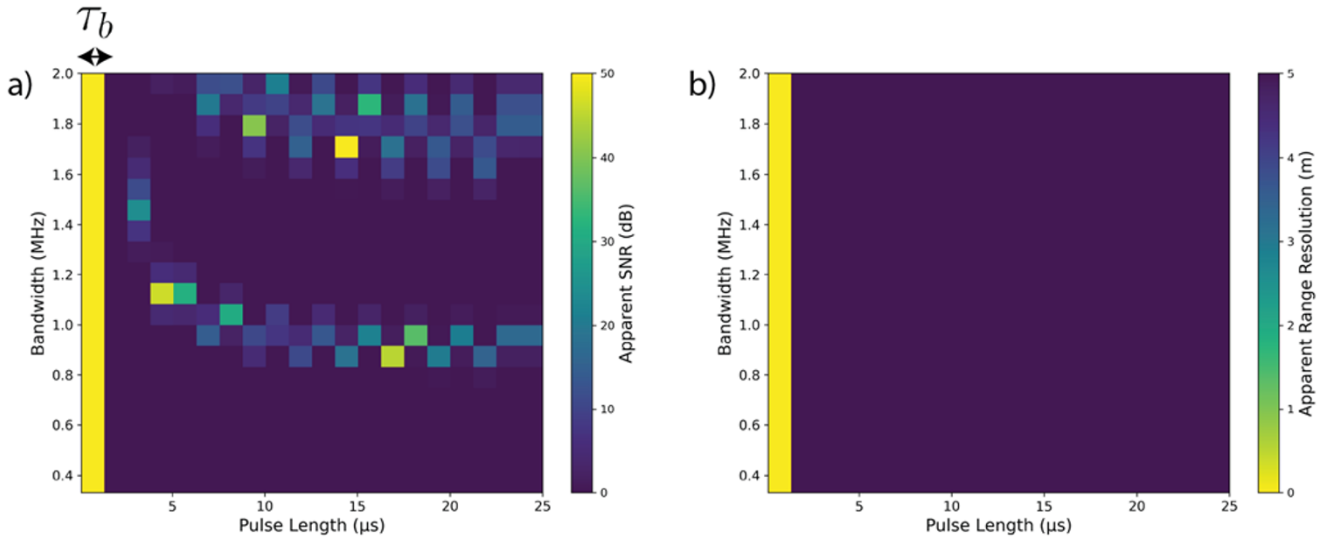


Figure 12. Performance of a ground-traversed sounder with a rectangular window ($\alpha = 0$). (a) The apparent SNR $[\mathrm{SNR}_a]$ and (b) apparent range resolution Δr_a as a function of bandwidth β and pulse length L. The target/platform parameters used in this scenario were $v = 10$ m/s, $h = 0$ m, $d = 100$ m, $\mathrm{SNR}_0 = 1$ dB, $\Delta P_r = 20$ dB, $f_c = 1$ MHz.

consistent with the design of the ApRES system (Brennan and others, 2014).

High SNR case

For the high SNR case, we employ a longer integration time by using a lower v of 0.0001 m/s, which corresponds to summing pulses over a few days. This longer integration time produces a higher SNR and moves the bed echo to a regime where $|R_s(\tau_b)|^2 > \langle P_{\mathrm{noise}} \rangle$. Figure 14 shows that for this scenario, the optimal choice looks more like the 'chirp' scenario in Fig. 10, with the maximum pulse length being set by τ_b. We note that this effect can also be produced by other sources of multiplicative noise like surface clutter, volume scatter and the matched-filter response on internal layers. While the specific pulse length threshold introduced by each will vary, shorter pulses will similarly mitigate these effects. Additionally, if speckle is the primary source of the multiplicative-noise limit, multilooking may offer additional mitigation (Long and Ulaby, 2015). The apparent range resolution remains optimized by having a signal with as wide a bandwidth as possible.

Discussion

Our results provide some clarity on why one might choose a particular type of radar or waveform for a particular observational scenario in glaciology. In addition, the absence of scenarios in which monotone pulse waveforms proved optimal suggests why some waveforms are no longer in widespread use. They also highlight the intrinsic and practical advantages of specific waveform choices as well as the processing and performance parameters underpinning them. It is our hope to move these from matters of practice to matters of analysis. Specifically, we discuss the role that duty cycle,

https://doi.org/10.1017/jog.2026.10210 Published online by Cambridge University Press

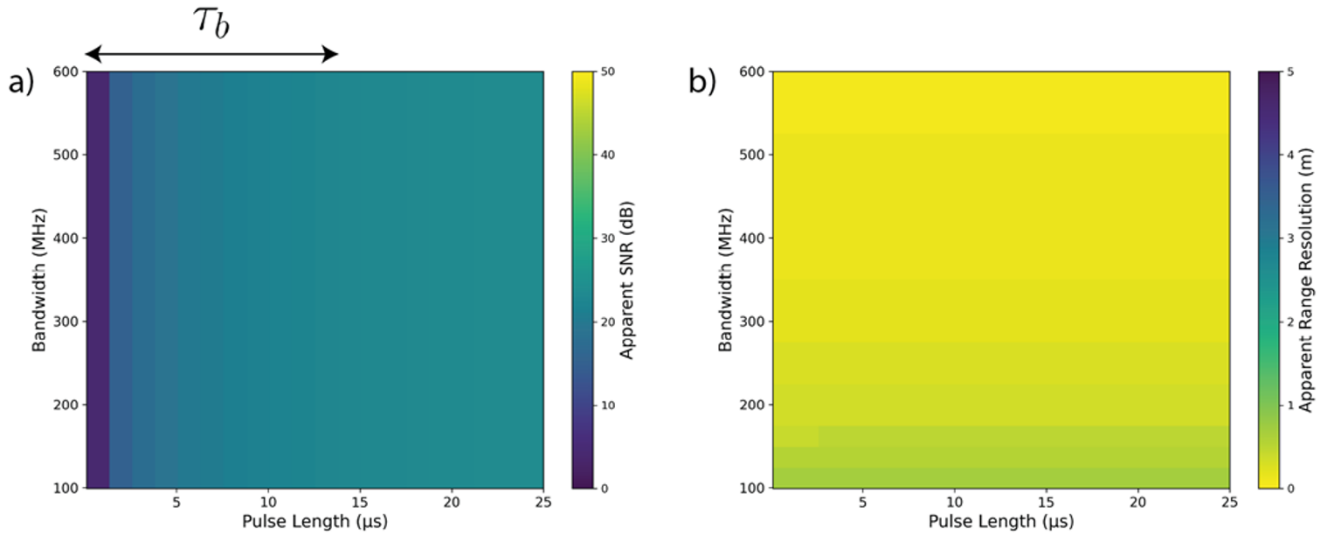


Figure 13. The performance of a stationary low-SNR ground-based CW sounder with a rectangular window ($\alpha = 0$) including (a) the apparent Signal-to-Noise Ratio $[\mathrm{SNR}_a]$ and (b) apparent range resolution Δr_a as a function of bandwidth β and pulse length L. The target/platform parameters used in this scenario were $v = 0.1$ m/s, $h = 0$ m, $d = 1.2$ km, $\mathrm{SNR}_0 = -50$ dB, $\Delta P_r = 40$ dB , $f_c = 300$ MHz.

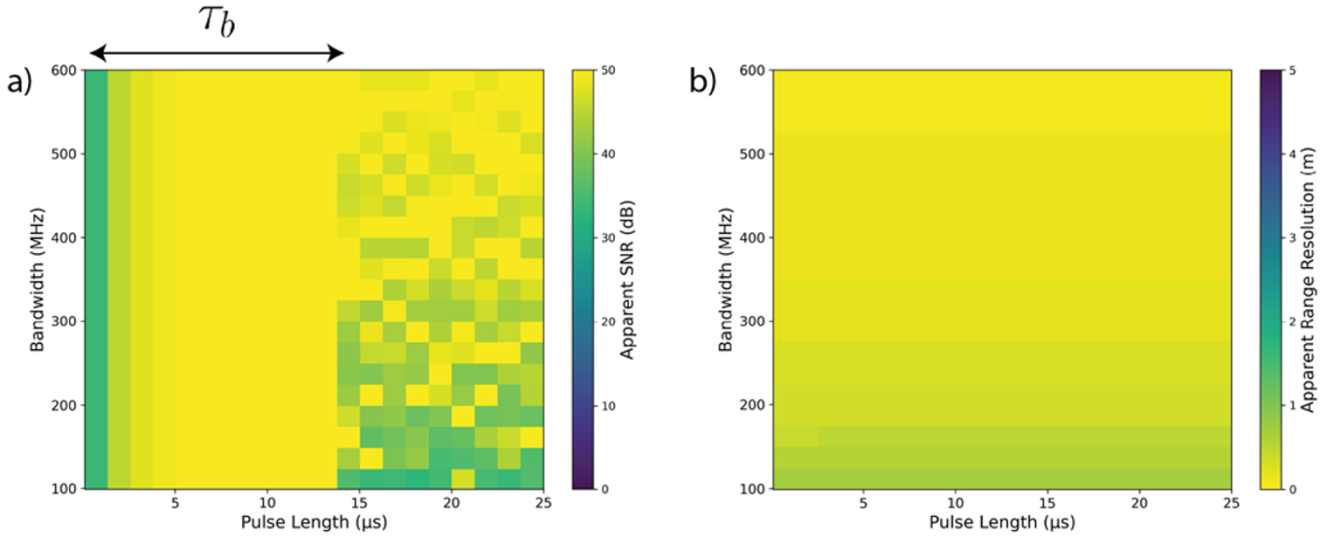


Figure 14. Performance of a stationary high-SNR ground-based CW sounder with a rectangular window ($\alpha = 0$) including (a) the apparent Signal-to-Noise Ratio $[\mathrm{SNR}_a]$ and (b) apparent range resolution Δr_a as a function of bandwidth β and pulse length L. The target/platform parameters used in this scenario were $v = 0.0001$ m/s, $h = 0$ m, $d = 1.2$ km, $\mathrm{SNR}_0 =$ -50 dB, $\Delta P_r = 40$ dB, $f_c = 300$ MHz.

pulse compression, coherent summation, matched-filter response and azimuth resolution play in detection, performance and waveform choice. We also discuss some examples and practical considerations for applying these insights to existing and future radar systems.

Duty cycle

One of the biggest differences between impulsive, chirped and CW radar waveforms is the portion of time that the radar is transmitting or their duty cycle D, given by

$$D = \mathrm{PRF} \cdot L. \tag{31}$$

This is particularly important when the link budgets are challenging due to high losses from propagation through ice or reflection from low-reflectivity subsurface interfaces. This need to overcome additive noise in ice-penetrating radar can be much more demanding than for many surface remote sensing systems (Schroeder and others, 2021). Although the exact tradeoffs will depend on range-resolution and acquisition geometries, CW radars will generally be capable of duty cycles closer to 100 percent, chirped radars closer to 10 percent and impulse radars closer to a small fraction of a percent (Arcone and others, 2004; Peters and others, 2007; Brennan and others, 2014). Excluding differences in pulse compression, post-processing SNR relative to additive noise will scale with those duty cycles. This means that the link budgets will be more favorable for higher duty cycle waveforms and could allow those systems to use lower power transmitters or operate on platforms with a higher speed or at higher altitude while achieving similar subsurface target SNR values. It could also mean that systems with higher

https://doi.org/10.1017/jog.2026.10210 Published online by Cambridge University Press

duty cycles could be used to detect more challenging subsurface targets. This is one of the reasons why a ground-traversed impulsive GPR might not detect subsurface targets in regions of thick or lossy ice where a ground-based or airborne chirped system may. As a result, if the only consideration was overcoming the detection limit of the additive noise floor, there would be every incentive to maximize the duty cycle pushing toward longer chirps or CW systems.

Pulse compression

Pulse compression gain G_c can also improve the detectability of bed echoes relative to an AGW noise floor. In Equation 21, we estimate that gain directly from the matched-filter response. However, in the literature, it is often cited as $\beta \cdot L$ because the energy in the transmitted pulse of length L is compressed to time range of approximately $1/\beta$. However, for an AGW noise floor, noise power also scales with β, so increasing the bandwidth will not improve the SNR of the bed echo. While SNR is indeed proportional to pulse length L, that gain is captured by Equation 31 in the discussion on Duty Cycle. As a result, increasing L will increase $[\mathrm{SNR}_a]$ insofar as it increases D and only if $|R_s(\tau_b)|^2 < \langle P_{\mathrm{noise}} \rangle$.

Coherent summation

Coherent summation gain from re-summing/stacking, unfocused SAR or focused SAR processing can also help overcome detection limits from $\langle P_{\mathrm{noise}} \rangle$ (Peters and others, 2007). In coherent summation, the in-phase signal amplitude increases like the number of summed traces N_t so that signal power increases like N_t^2. In contrast, the RMS amplitude of the noise floor σ_n increases like $\sqrt{N_t}$ so that the noise power increases like N_t. As a result, the SNR increases in proportion to N_t (Bienert and others, 2020). We note that any of the waveform types we consider can enjoy coherent processing gain if their timing between transmit and receive is stable enough to result in a stable phase trace $\phi(\tau)$ across pulses (Gogineni and others, 1998). It also follows that all coherent systems are 'phase sensitive' in that they can measure echo phase change or perform interferometry and that capability is not inherent or limited to any particular instrument or waveform type. Unlike the discussion of pulse length, there generally is no downside to greater coherent summation unless it results in destructive interference in sloped layer signals or reduces the effective PRF to the point of Doppler aliasing (Raney, 2002; Holschuh and others, 2014). However, as above, it is possible to hit a point where the record is limited by multiplicative noise and additional coherent summation no longer improves the detectability of subsurface targets once $|R_s(\tau_b)|^2 > \langle P_{\mathrm{noise}} \rangle$.

Matched-filter response

Our general, waveform-agnostic approach to processing ice-penetrating radar allowed us to focus our analysis on the intrinsic performance potential of the waveforms themselves rather than of the particular implementation with which they are realized in existing radar systems. It also offers some interesting opportunities to reframe how we think about some features of those signals and systems. For example, the phenomena of range sidelobes and pulse compression can be seen as two emergent features describing the shape of the waveform matched-filter response $R_s(\tau)$ relative to the transmitted waveform $s(t)$. Similarly, the obscuring effect of both the sidelobes and the main lobe of stronger shallower returns on bed echoes can be seen as particular expressions of the general obscuring effect of total matched-filter $R_s(\tau)$. For the purpose of this paper, we focused on the surface as the source of bed detection limiting matched-filter response. However, englacial layers, water, debris and off-nadir basal topography as well as direct-path signals all have the potential to introduce detection limiting matched-filter responses with similar implications on waveform choices. The main takeaways from the results of this paper in terms of matched-filter response are:

- 1) It matters and can be a limiting factor in ice-penetrating radar performance.
- 2) There are targets for which the matched-filter response is the dominant limit and, as a result, systems with better matched-filter response performance like shorter chirps or impulsive waveforms are often chosen at these study sites, either explicitly or implicitly, for this reason.
- 3) These results raise the possibility that ice-penetrating radars can hit a point where additional coherent summation no longer increases the apparent SNR because the subsurface target has moved from a noise-limited to a matched-filter-response-limited regime.

This last item is an interesting and provocative result. It suggests that stationary systems which have the opportunity for longer deployment may benefit from shifting waveforms from CW-type to chirp-like waveforms. In the extreme scenario of very long deployments with targets that include englacial and subglacial returns across a variety of depths, it would even suggest that very short chirps or even impulse-like waveforms could be optimal. The SNR-maximizing property of matched filtering applies to all deterministic waveforms in the presence of additive Gaussian white noise, so the processing pipeline in Fig. 7 represents a plausible implementation of impulsive and CW ice-penetrating radars. In the case of impulsive waveforms, this would result in little to no pulse-compression gain and may even widen pulses. In the case of CW waveforms, a system with sufficiently capable waveform generators and digitizers could transmit and record the full waveform and implement matched-filtering in software. This raises exciting potential for development of new long-duration non-CW systems for ground-based observation based on Software Defined Radios (Teisberg and others, 2024).

Azimuth resolution and clutter mitigation

The previous sub-sections have focused on the relative roles of the noise floor and matched-filter response in limiting subsurface target detection. An additional secondary consideration in waveform choice is the azimuth resolution. For sounding geometries where subsurface echoes are often dominated by coherent/specular returns, the azimuth resolution can, in many cases, be set by the Fresnel Zone diameter D_f

$$D_f = \sqrt{2\lambda(h + d/\sqrt{\epsilon_i})}. \tag{32}$$

In other cases it can be determined by the along-track processing aperture L_{app} so that the azimuth resolution δ_{az} is given by

$$\delta_{az} = \frac{\lambda h}{2L_{app}} \tag{33}$$

Peters and others (2007). In both cases, the azimuth resolution is a function of center frequency and is either proportional to λ for

https://doi.org/10.1017/jog.2026.10210 Published online by Cambridge University Press

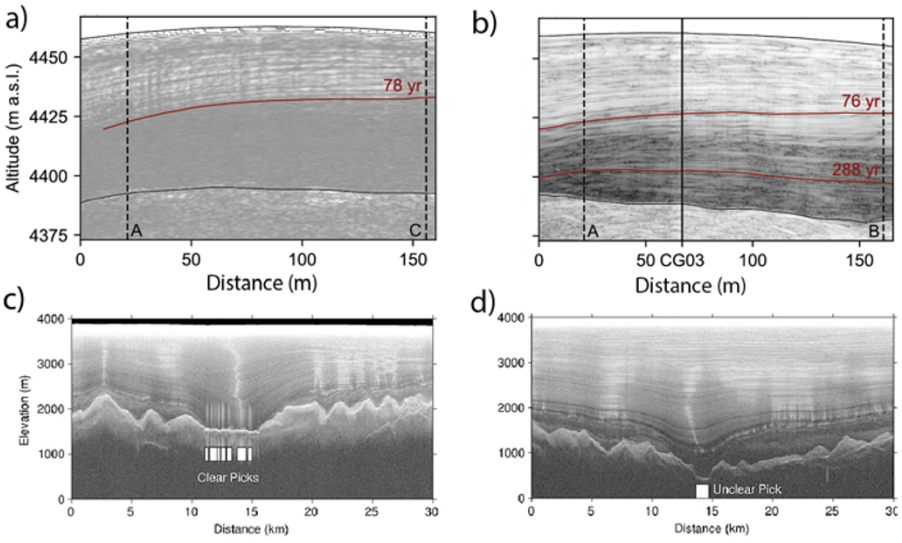


Figure 15. Example radargrams illustrating some of the effects discussed in this paper. Both (a) impulse and (b) CW data from an alpine glacier showing deep layers visible in the CW data limited by the noise floor in the impulse data (adapted from Oraschewski and others (2024)). Both (c) high SNR and (d) low SNR chirped data with rectangular windowing in which the matched-filter response of high SNR bed echoes has the potential to obscure weaker nearby echoes (e.g. the bright vertical lines above the 'clear picks' boxes in the figure) and low SNR bed echoes that do not (adapted from Wolovick and others (2013)).

the focused case or $\sqrt{\lambda}$ for the Fresnel-Zone limited case. As a result, systems with carrier frequencies like chirped or CW systems will have better azimuth resolutions than impulse systems with the same range resolution.

Practical considerations for existing and future systems

While our analysis intentionally focused on the intrinsic theoretical potential performance properties of waveforms themselves, Fig. 15 shows that the radioglaciology literature illustrates many of the phenomena highlighted in our analysis. This includes examples, like Fig. 15a and 15b, where systems with impulsive waveforms fail to detect faint layers above the noise floor that are visible in CW data. It also includes examples, like Fig. 15c and 15d, where the matched-filter response of bed echoes produces strong near-bed side-lobes with the potential to obscure shallower faint echoes that may exist near the bed when the bed SNR is high.

Additionally, the choice facing field-going glaciologists is often between distinct radar systems and their particular implementations of these waveforms rather than of the waveforms themselves. For example, many widely-used commercial impulsive GPR systems employ triggering and digitizing systems with excessive jitter so that coherent summation-gain, phase-based analysis and focusing processing may not be possible. Further, the very favorable matched-filter response of impulse-like waveforms often comes at the cost of unworkable link budgets due to very low duty cycles. For stationary or traversed platforms, it is possible for integration times to span minutes to days so that coherent processing gain may be able to compensate for duty cycle. However, for faster-moving airborne or satellite systems this option is not available. Similarly, the waveform-shaping flexibility of non-saturating transmitters that enable windowing the transmitted signal typically comes at a price in terms of power, efficiency or weight. This trade-off may be tolerable for some platforms and targets but not for others.

In other cases, field campaigns may be studying targets that are better suited to chirped waveforms in the thick lossy interior of an ice sheet, but may default to more widely available commercial impulsive GPRs in the absence of access to or familiarity with ground-based traversable chirped systems.

In terms of systems using CW waveforms, nearly all existing systems mix their transmitted signals with the received signal in order to reduce the requirements on digitizer bandwidth and data volume. For many practical glaciological settings, the limited information loss and reduction in waveform shaping flexibility associated with this implementation is an easy trade to make; these systems are high heritage, low cost, low power and require minimal data storage or processing power. However, as our results show, there are cases in which these CW deployments can cross over from noise-limited to matched-filter-response limited regimes. In those cases, chirped or coherent impulsive systems may be required to drive the detection threshold lower.

Conclusion

The point of view we hoped to put forward in this paper is that ice-penetrating radar systems can be viewed as part of a continuum determined by the parameters of their waveforms. We show that CW, impulsive and chirped waveforms are each suited to the targets and acquisition geometries in which they are most widely used. We also note that coherent implementations of all three types of waveforms are capable of increasing their SNR with coherent summation and of performing phase-based analysis as a result of the often-overlooked fact that all coherent radar systems are 'phase-sensitive'. We also illustrate that some observing scenarios can move ice-penetrating radar from a noise-floor limited regime to a matched-filter response limited regime motivating a change in strategy from increasing duty cycle to shortening waveform lengths. Finally, we show that, for long deployments, stationary radar sounders that can adapt their transmitted signal from CW to chirped or even to impulse-like waveforms have the potential to unlock dramatically improved imaging of subsurface targets by optimizing their waveform for the target scene.

Supplementary material. The supplementary material for this article can be found at https://doi.org/10.1017/jog.2026.10210

https://doi.org/10.1017/jog.2026.10210 Published online by Cambridge University Press

Acknowledgements. This work was supported, in part, by a grant from the W.M. Keck Foundation. We also thank R. Drews and J. Noll for their exceptionally thoughtful, detailed and constructive reviews.

References

Allen C (2008) A brief history of radio-echo sounding of ice. *Earthzine Month. Newsl*.

Arcone SA, Spikes VB, Hamilton GS and Mayewski PA (2004) Stratigraphic continuity in 400MHz short-pulse radar profiles of firn in West Antarctica. *Annals of Glaciology* **39**, 195–200.

Arenas-Pingarrón A, Corr HF, Robinson C, Jordan TA and Brennan PV (2023) Polarimetric airborne scientific instrument, mark 2, an ice-sounding airborne synthetic aperture radar for subglacial 3D imagery. *IET Radar, Sonar & Navigation* **17**(9), 1391–1404.

Arnold E and 6 others (2020) Cresis airborne radars and platforms for ice and snow sounding. *Annals of Glaciology* **61**(81), 58–67.

Bailey J, Evans S and GdQ R (1964) Radio echo sounding of polar ice sheets. *Nature* **204**(4957), 420–421.

Bienert NL, Schroeder DM, Peters ST and Siegfried MR (2020) Processing-based synchronization approach for bistatic radar glacial tomography. In *IGARSS 2020-2020 IEEE International Geoscience and Remote Sensing Symposium*, IEEE, pp. 1420–1423.

Björnsson H and Pálsson F (2020) Radio-echo soundings on Icelandic temperate glaciers: History of techniques and findings. *Annals of Glaciology* **61**(81), 25–34.

Blankenship DD and 10 others (2024) Radar for Europa assessment and sounding: Ocean to near-surface (reason). *Space Science reviews* **220**(5), 51.

Brennan PV, Lok LB, Nicholls K and Corr H (2014) Phase-sensitive FMCW radar system for high-precision Antarctic ice shelf profile monitoring. *IET Radar, Sonar & Navigation* **8**(7), 776–786.

Christensen EL, Gundestrup N, Nilsson E and Gudmandsen PE (1970) *Radioglaciology 60 MHz radar*, Technical University of Denmark, Laboratory of Electromagnetic Theory.

Dall J (2010) Ice sheet anisotropy measured with polarimetric ice sounding radar. In *2010 IEEE International Geoscience and Remote Sensing ymposium*, IEEE, pp. 2507–2510.

Gogineni S, Chuah T, Allen C, Jezek K and Moore RK (1998) An improved coherent radar depth sounder. *Journal of Glaciology* **44**(148), 659–669.

Holschuh N, Christianson K and Anandakrishnan S (2014) Power loss in dipping internal reflectors, imaged using ice-penetrating radar. *Annals of Glaciology* **55**(67), 49–56.

Long D and Ulaby F (2015) *Microwave Radar and Radiometric Remote sensing.*, Artech.

Mingo L, Flowers GE, Crawford AJ, Mueller DR and Bigelow DG (2020) A stationary impulse-radar system for autonomous deployment in cold and temperate environments. *Annals of Glaciology* **61**(81), 99–107.

Nicholls KW, Corr HF, Stewart CL, Lok LB, Brennan PV and Vaughan DG (2015) A ground-based radar for measuring vertical strain rates and time-varying basal melt rates in ice sheets and shelves. *Journal of Glaciology* **61**(230), 1079–1087.

Oraschewski FM, Koch I, Ershadi MR, Hawkins JD, Eisen O and Drews R (2024) Layer-optimized synthetic aperture radar processing with a mobile phase-sensitive radar: A proof of concept for detecting the deep englacial stratigraphy of Colle Gnifetti, Switzerland and Italy. *The Cryosphere* **18**(8), 3875–3889.

Paden J, Akins T, Dunson D, Allen C and Gogineni P (2010) Ice-sheet bed 3-D tomography. *Journal of Glaciology* **56**(195), 3–11.

Peters ME, Blankenship DD, Carter SP, Kempf SD, Young DA and Holt JW (2007) Along-track focusing of airborne radar sounding data from west antarctica for improving basal reflection analysis and layer detection. *IEEE Transactions on Geoscience and Remote Sensing* **45**(9), 2725–2736.

Peters S and 6 others (2021) Glaciological monitoring using the sun as a radio source for echo detection. *Geophysical Research Letters* **48**(14), e2021GL092450.

Pritchard HD and 10 others (2025) Bedmap3 updated ice bed, surface and thickness gridded datasets for Antarctica. *Scientific data* **12**(1), 414.

Raney RK (2002) The delay/doppler radar altimeter. *IEEE Transactions on Geoscience and Remote Sensing* **36**(5), 1578–1588.

Robin G de Q, Drewry D and Meldrum D (1977) International studies of ice sheet and bedrock. *Philosophical Transactions of the Royal Society of London. B, Biological Sciences* **279**(963), 185–196.

Rodriguez-Morales F and 10 others (2013) Advanced multifrequency radar instrumentation for polar research. *IEEE Transactions on Geoscience and Remote Sensing* **52**(5), 2824–2842.

Scanlan KM, Rutishauser A, Young DA and Blankenship DD (2020) Interferometric discrimination of cross-track bed clutter in ice-penetrating radar sounding data. *Annals of Glaciology* **61**(81), 68–73.

Schroeder DM and 6 others (2021) Glaciological constraints on link budgets for orbital radar sounding of Earth's ice sheets. In *2021 IEEE International Geoscience and Remote Sensing Symposium IGARSS*, IEEE, pp. 647–650.

Schroeder DM and 9 others (2020) Five decades of radioglaciology. *Annals of Glaciology* **61**(81), 1–13.

Teisberg TO, Broome AL and Schroeder DM (2024) Open radar code architecture (ORCA): A platform for software-defined coherent chirped radar systems. *IEEE Transactions on Geoscience and Remote Sensing* **62**, 1–11.

Wolovick MJ, Bell RE, Creyts TT and Frearson N (2013) Identification and control of subglacial water networks under Dome A, Antarctica. *Journal of Geophysical Research: Earth Surface* **118**(1), 140–154.

https://doi.org/10.1017/jog.2026.10210 Published online by Cambridge University Press